Journal of the Meteorological Society of Japan, Vol. 87, No. 4, pp. 771–789, 2009.
DOI:10.2151/jmsj.87.771

Evaluation of Precipitation and High-Level Cloud Areas Associated with Large-Scale Circulation over the Tropical Pacific in the CMIP3 Models

Hiroki ICHIKAWA

Department of Earth and Environmental Sciences, Graduate School of Environmental Studies, Nagoya University, Nagoya, Japan

Hirohiko MASUNAGA

Hydrospheric Atmospheric Research Center, Nagoya University, Nagoya, Japan

and

Hiroshi KANZAWA

Department of Earth and Environmental Sciences, Graduate School of Environmental Studies, Nagoya University, Nagoya, Japan

(Manuscript received 29 September 2008, in final form 23 April 2009)

Abstract

Precipitation and high-level cloud (HLC) areas in association with the large-scale circulation over the tropical Pacific are analyzed for simulations of nineteen Coupled Model Intercomparison Project Phase 3 (CMIP3) models with observations for 16 years of 1984–1999. The distribution of rainfall and HLC areas are composited around the geographical center of tropospheric upper-level (200 hPa) divergence (DIV) along Intertropical Convergence Zone (ITCZ) using monthly anomaly data. Datasets with a finer temporal sampling than monthly means were not available for the present purposes. The most notable feature is that the horizontal spread of enhanced circulation and the related rainfall and HLC areas are all underestimated around the DIV center in the models compared to the observation. Particularly, the underestimation is pronounced in HLC, presumably owing to difficulties in the physical processes relevant to the spatial distribution of HLC area. In general, a model with a higher correlation between the large-scale circulation field and rainfall tends to have a wider spread of HLC area around the DIV center.

1. Introduction

Deep and frequent convection and the associated precipitation over the tropics activate the vigorous hydrological cycle in the earth climate system. A huge amount of latent heat release associated with the convection and precipitation makes the tropical region a major atmospheric heat source (e.g., Yanai and Tomita 1998) that plays an essential role in driving global general circulation. The better understanding of spatio-temporal cloud/rainfall variability and its background dynamical/thermodynamical mechanism would help improve the current skill in the climate model for reproducing the present and past climate and for predicting the future climate change.

Tropical deep convection and the associated precipitation respond both to large-scale dynamical

Corresponding author: Hiroki Ichikawa, Department of Earth and Environmental Sciences, Graduate School of Environmental Studies, Nagoya University, Furo-cho, Chikusa-ku, Nagoya 464-8601, Japan.
E-mail: ichikawa@hyarc.nagoya-u.ac.jp

forcing and local thermodynamic changes. Because the large-scale circulation is tied to the pattern of underlying sea surface temperature (SST) that slowly varies from a season to another, deeper convection and heavier rainfall occur over regions with higher SST and stronger upward motion (e.g., Del Genio and Kovari 2002), accounting for visible appearance of Intertropical Convergence Zone (ITCZ) in satellite imagery. Over the western and central Pacific ITCZ regions, deep convection systems accompany more abundant anvil cirrus clouds compared to the eastern Pacific region for a given rainfall rate (Hartmann et al. 2001; Kubar et al. 2007). The cloud-circulation-SST relationships characterize the regional difference of convection/rainfall systems along the Pacific ITCZ (Hartmann et al. 2001; Berg et al. 2002; Masunaga et al. 2005; Back and Bretherton 2006; Kubar et al. 2007).

The representation of cloud and precipitation in the climate models has been a big challenge to the climate research community. Dai (2006) analyzed the temporal and horizontal variation of precipitation in the latest generation of coupled Atmosphere-Ocean General Circulation Models (AOGCMs), and revealed that most models reproduced the observed broad spatial pattern and year-to-year variability of precipitation. On the other hand, the models fail to differentiate precipitation types in a realistic manner, with too much convective precipitation compared with the Tropical Rainfall Measuring Mission satellite observation in the tropics and subtropics. While it is difficult to compare precipitation types in the models depending on convection schemes with those in the satellite estimate depending on the original algorithm, the comparison of precipitation types would be conveyed in useful information. Zhang et al. (2005) evaluated the cloud property in several Atmospheric General Circulation Models (AGCMs), and found the significant biases where optically intermediate and thin clouds are underestimated while thick clouds are overestimated. Compensation of the errors in representing cloud fraction at various heights and cloud thickness in the models results in relatively good representation in radiative flux at the top of the atmosphere. Associated with the deficiency of a well-stacked cloud layer, the models tend to simulate the cloud albedo moderately well, but not the cloud water path (Wear 2004).

How the tropical climate system responds to an external forcing is an important outstanding problem (e.g., Stephens 2005). A recent satellite observation indicated that the deep convective activity over the ocean with SST above $\sim$27–28°C greatly enhances the upper-tropospheric water vapor greenhouse effect (Su et al. 2006a). The latest AOGCMs well simulate qualitatively the observed relationships of larger amount of upper-level ice clouds and water vapor with higher SST, but they quantitatively disagree with the observation and each other (Su et al. 2006b). For the climate models, clouds and precipitation associated with tropical convection should be further evaluated because they play a determining role in the global general circulation and hydrological cycle that eventually influence them.

In this study, precipitation and high-level cloud areas associated with large-scale circulation mainly in the horizontal pattern over the Pacific Ocean in coupled AOGCMs are evaluated. Previously, the evaluation of clouds and precipitation in the climate model has been made on a global or zonal-mean basis (e.g., Dai 2006; Zhang et al. 2005), or using regime-sorted approaches (e.g., Bony et al. 2004; Wyant et al. 2006; Williams and Tsekioudis 2007) on the climatological mean basis. While the climatological mean pattern of rainfall in the latest AOGCMs has been evaluated by Dai (2006), that of high-level clouds and large-scale circulation, and the linkage of rainfall and high-level cloud with large-scale circulation has not been evaluated yet. First, this study evaluates the climatological mean relationships of rainfall and high-level cloud areas with large-scale circulation. However, the direct intercomparisons of climatological mean fields alone are not necessarily informative to a suitable evaluation of physics in the climate model. Here we focus on the interaction of rainfall and high-level cloud areas with large-scale circulation associated with subseasonal disturbances that are defined as disturbances on a time scale shorter than a season but longer than a few weeks, and analyze the spatial linkage of rainfall and high-level cloud areas with the large-scale circulation associated with the disturbances. In order to accomplish the purpose, we investigate the horizontal patterns of rainfall and high-level cloud areas around large-scale divergence centers in the upper-troposphere in association with subseasonal disturbances through a composite analysis. Large-scale circulation associated with subseasonal disturbances may have a strong impact on seasonal-to-climatological mean large-scale circulation. The relationship of reproducibility

of the climatological mean field with that of subseasonal disturbances in the models is finally discussed.

The paper is organized as follows. Section 2 outlines the data used in this study and provides a brief overview of climate models. In Section 3, first, general features of the climatological mean of rainfall and high-level cloud areas in the models are evaluated (Section *3.1*). Second, the composite patterns of rainfall and high-level cloud areas associated with large-scale circulation are analyzed for the observation and models (Section *3.2*). Third, the reproducibility of the climatological mean field and that of subseasonal disturbances in the models are compared (Section *3.3*). Section 4 presents a summary and discussion.

2. Data and methods

2.1 Observational and reanalysis data

The data used in this study includes the international satellite cloud climatology project (ISCCP) D2 VIS/IR cloud data (Rossow and Schiffer 1999), obtained from the NASA Langley Research Center Atmospheric Science Data Center. The data contain the monthly mean cloud fraction for three height categories. In particular, high clouds with top pressures between 440 and 50 hPa are used in this study to investigate the variability of upper-tropospheric clouds. The high clouds are further classified into three cloud types; deep convection (DC), cirrostratus (CS), and cirrus (CI) on the basis of the optical thickness in the product. The high level cloud (HLC), defined as these three types of clouds all together, is analyzed in most of this paper, but each classified cloud (DC, CS, CI) is partly analyzed for the physical interpretation of observational evidence. The observed precipitation from Global Precipitation Climatology Project (GPCP) (Adler et al. 2003) is utilized. The large-scale circulation field is derived from European Centre for Medium-Range Weather Forecasts (ECMWF) ERA-40 reanalysis data (Uppala et al. 2005). The outgoing longwave radiation (OLR) datasets (Liebmann and Smith 1996) and monthly mean SST using optimum interpolation (Reynolds and Smith 1994), both of which are distributed by the National Oceanic and Atmospheric Administration (NOAA) Climate Prediction Center (CPC), are also used. For comparisons with AOGCMs outputs, all these data with the same horizontal resolution of $2.5^\circ \times 2.5^\circ$ grid on a monthly average are used for 16 years of 1984–1999, limited by the observational period of ISCCP.

2.2 AOGCMs simulations

This study uses the outputs from the twentieth-century climate simulations conducted by 19 AOGCMs listed in Table 1. At the time of writing, only these 19 model outputs make three dimensional cloud amounts available among the registered 25 model outputs. Our analysis is based on the monthly mean data, because cloud amount is not available for a finer temporal sampling than monthly means. These models participated in the Fourth Assessment Report (AR4) of the Intergovernmental Panel on Climate Change (IPCC) (IPCC 2007), and their data were submitted to Program for Climate Model Diagnosis and Intercomparison (PCMDI). These archived data constitute phase 3 of the World Climate Research Programme (WCRP) Coupled Model Intercomparison Project (CMIP3).

The spatial resolution of model ranges from the highest resolution of $1.1^\circ \times 1.1^\circ$ (MIROC3.2-hires) to the lowest resolution of $5.0^\circ \times 4.0^\circ$ (GISS-EH/ER). Most of the models do not use the surface flux corrections except for 4 models (CCCMA-CGCM3.1-t47/t63, INMCM3.0, MRI-CGCM2.3.2a). Clouds and precipitation associated with tropical convection are strongly affected by convection schemes adopted in the models. In most models analyzed in this study, the adopted parameterizations are based on Arakawa and Schubert (1974) or bulk flux schemes while the final implementations are different from a model to another (see for details Table 2 in Dai 2006). In the model using the Arakawa-Schubert scheme, MIROC3.2-hires/medres and MRI-CGCM2.3.2a use prognostic cumulus kinetic energy as a closure while GFDL-CM2.0/2.1 use relaxed quasi-equilibrium between large-scale forcing and convection. In the bulk flux scheme, stability-dependent closure is adopted in three models of CSIRO-MK3.5, GISS-EH/ER, and UKMO-HadCM3, while the original Kuo-type moisture convergence is used in a model of BCCR-BCM2.0. The Zhang and McFarlane (1995) scheme, used by CCCMA-CGCM3.1, IAP-FGOALS-g1.0, NCAR-CCSM3.0, and NCAR-PCM1, is designed primarily for well reproducing deep convection and adopts the consumption of convective available potential energy (CAPE) by convection as a closure. Additionary, further modifications such as relative humidity suppression applied in MIROC3.2 (Emori et al. 2001) have been made in most of the models. More information on aspects of the physical pa-

Table 1. Description of 19 coupled AOGCMs, the output data of which are analyzed in this study. For more information such as resolution of the ocean, see http://www-pcmdi.llnl.gov/.

Label	Model name	Resolution (Atmosphere) (horizontal/vertical)	References
a	BCCR-BCM2.0	1.9° × 1.9° / L31	Deque et al. (1994)
b	CCCMA-CGCM3.1-t47	2.8° × ∼2.8° / L31	Flato (2000)
c	CCCMA-CGCM3.1-t63	1.9° × ∼1.9° / L31	Flato (2000)
d	CSIRO-MK3.5	1.9° × ∼1.9° / L18	Gordon et al. (2002)
e	GFDL-CM2.0	2.5° × 2.0° / L24	Delworth et al. (2006)
f	GFDL-CM2.1	2.5° × 2.0° / L24	Delworth et al. (2006)
g	GISS-EH	5.0° × 4.0° / L20	Schmidt et al. (2006)
h	GISS-ER	5.0° × 4.0° / L20	Schmidt et al. (2006)
i	IAP-FGOALS-g1.0	2.8° × ∼2.8° / L26	Yu et al. (2004)
j	INGV-ECHAM4	1.1° × 1.1° / L19	Gualdi et al. (2006)
k	INMCM3.0	5.0° × 4.0° / L21	Diansky and Volodin (2002)
l	IPSL-CM4	3.75° × 2.5° / L19	Marti et al. (2005)
m	MIROC3.2-hires	1.1° × ∼1.1° / L56	K-1 model developers (2004)
n	MIROC3.2-medres	2.8° × ∼2.8° / L20	K-1 model developers (2004)
o	MPI-ECHAM5	1.9° × ∼1.9° / L31	Roeckner et al. (2003)
p	MRI-CGCM2.3.2a	2.8° × ∼2.8° / L30	Yukimoto et al. (2006)
q	NCAR-CCSM3.0	1.4° × 1.4° / L26	Collins et al. (2006)
r	NCAR-PCM1	2.8° × ∼2.8° / L26	Washington et al. (2000)
s	UKMO-HadCM3	3.75° × 2.5° / L19	Gordon et al. (2000)

rameterization can be found in Dai (2006).

The twentieth century simulations by AOGCMs are evaluated by using monthly mean outputs for 1984–1999 so that the data period matches that of the satellite observation. All the variables are interpolated to the common 2.5 × 2.5 grid, the same as the observational data set.

2.3 *Cloudiness in the observation and model simulations*

Comparing cloudiness of the observation with that of model outputs is challenging because of large differences in nature between the two. One of the fundamental problems for the comparison is that the models are run at far lower horizontal resolutions than the 4–10 km pixel of the raw ISCCP data. Clouds in the models need to be parameterized from the prognostic grid-mean variables such as the upward mass flux and/or the relative humidity of the grid box. In addition, the definition of cloudiness in the models using a threshold of cloud water/ice concentration or an optical depth of the cloud condensate is not consistent with that in the observation. Given these limitations in the model representation of cloudiness, cloud radiative effect (CRE) might be a suitable measure for the comparison between the observation and the models. However, the evaluation of CRE does not necessarily provide the physical insight on particular model biases arising from individual types of clouds because CRE only measures the accumulative effects of clouds.

This study tries to evaluate clouds in the models. Several objective methods for quantitatively characterizing the clouds in the models have been developed. The ISCCP simulator, which stratifies the

model's cloud types into the same cloud types as ISCCP using the model's radiation scheme, is one of the major tools for evaluating clouds in the models (e.g., Klein and Jakob 1999; Webb et al. 2001). However, ISCCP simulator needs to be run online with the model run itself, but the online run products are unavailable for our analysis. This study adopts, therefore, the method of maximum overlap assumption developed by Wear (2004) for defining HLC. The method has been used for evaluating clouds in climate models (e.g., Karlsson et al. 2008). In the models, cloud fraction has been given by the modeling groups at fixed pressure levels which vary from a model to another. In order to compare the model output with the ISCCP observation as seen from satellites, model cloud fraction has to be dealt with in a way consistent with the observation. Concretely, the HLC amount is defined as the largest value of cloud fraction among all levels with pressures between 440 and 50 hPa. The detection of HLC by this definition closely follows the HLC of the ISCCP estimate. Unfortunately, cloud type classification such as DC, CS, and CI as in ISCCP cannot be made because of the unavailability of information about optical thickness in the models. The model outputs and ISCCP estimate are, thus, compared for HLC without being further divided into subcategories. The maximum overlap assumption has the advantage that the results are nearly independent of the differences between model radiation codes.

While the detected HLC for the models is considered to follow the HLC of the ISCCP estimate, it is difficult to evaluate the HLC for the models exactly because of a large difference in the nature of cloudiness between the observation and the models as is described above. Considering the limitation in the model representation of cloudiness, OLR is also analyzed as well as HLC in the composite analysis in Section 3.2 as a more objective measure for the comparison between the observation and the models.

3. Results

3.1 General features of climatological mean precipitation and high-level cloud areas

a. Spatial patterns

First of all, observational climatologies of rainfall and high-level cloud areas are analyzed and compared with AOGCMs outputs.

Figure 1a shows the observed spatial distribution of annual mean rainfall area from GPCP for 16 years (1984–1999). Divergence at 200 hPa, hereafter designated by DIV (white solid contours), and SST at 27°C (a black dotted contour) are superposed. The DIV, associated with the tropical large-scale circulation, is closely related to SST in the climatological mean pattern because changes in large-scale upward motion, inducing DIV, often occur in association with changes in the spatial distribution of SST (e.g., Lindzen and Nigam 1987). Areas with intense rainfall in the tropics are strongly related to the large-scale circulation field as inferred by DIV. Particularly, heavily raining areas are observed over the Maritime Continent, Pacific ITCZ, and South Pacific Convergence Zone (SPCZ). The spatial distribution of each type of high-level cloud areas is shown in Fig. 1b (DC) and 1c (CI) for comparison with that of the rainfall area. The distribution of DC area (Fig. 1b) resembles the distribution of the rainfall area (Fig. 1a), indicating that most of the rainfall is yielded by

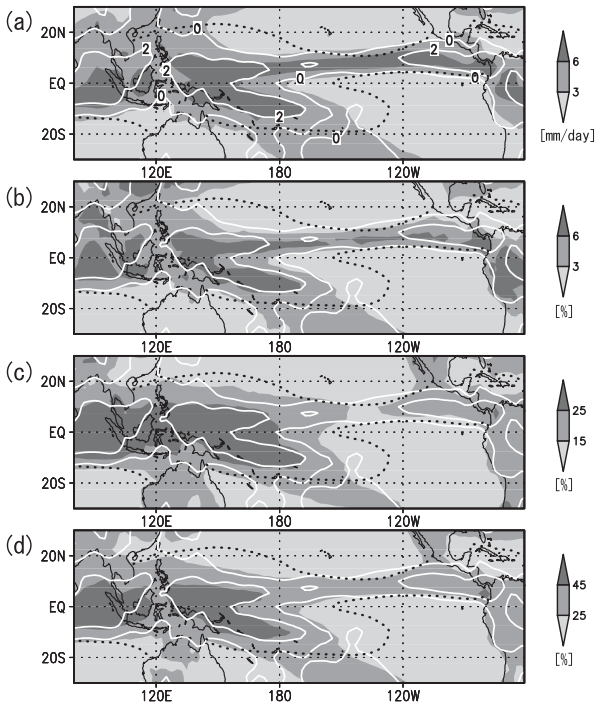

Fig. 1. Annual mean (1984–1999) spatial distribution of (a) Rainfall, (b) DC, (c) CI, and (d) HLC (in grey scale). DIV (divergence at 200 hPa) is shown by white solid contours with 0.0, 2.0 [$\times 10^{-6}$ s^{-1}]. SST at 27°C is indicated by a black dotted contour.

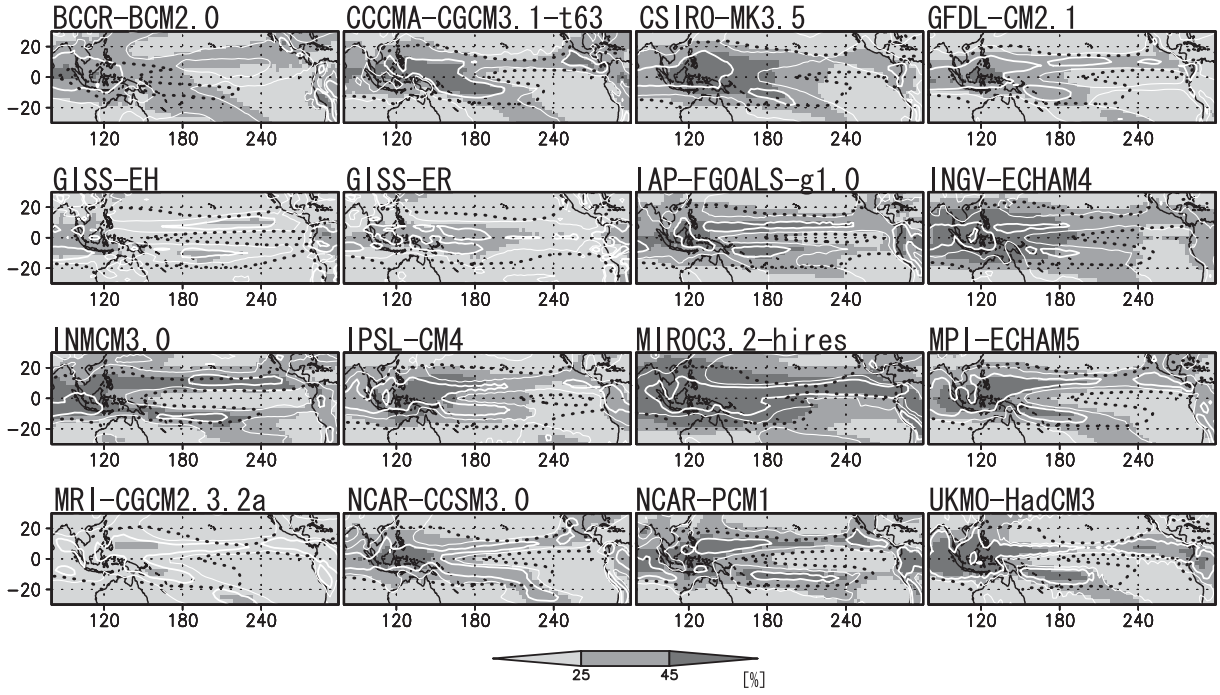

Fig. 2. Same as Fig. 1d but for selected 16 coupled AOGCMs among 19 models. Three models of CCCMA-CGCM3.1-t47, GFDL-CM2.0, and MIROC3.2-medres are not shown because the spatial patterns of these 3 models are similar to the other version of the same models (i.e., CCCMA-CGCM3.1-t63, GFDL-CM2.1, and MIROC3.2-hires).

deep convective clouds. Particularly, the DC amount is large over the western to central/south-central Pacific, mostly confined in the region with strong DIV (contour at 2×10^{-6} s^{-1}). Spatial characteristics similar to DC area can also be observed in the distribution of CS area (not shown). On the other hand, the distribution of CI area (Fig. 1c) is more widely spread from the Indian Ocean to the Pacific than that of the other types of high-level cloud and rainfall areas. CI area does not exceed 25% in amount over the eastern Pacific. Figure 1d shows the annual mean distribution of HLC area, that is, the summation of DC, CS, and CI areas. HLC area is enlarged along ITCZ and SPCZ as visualized by the heavily raining area and large DIV region of Fig. 1a, particularly over the western Pacific where DIV is also strong.

Here, we briefly analyze the mean spatial pattern of HLC area in AOGCMs. The annual mean spatial distributions of HLC area (in grey scale), DIV (white solid contours), and SST (a black dotted contour) are shown in Fig. 2. As inferred from the DIV field, the models well simulate the overall large-scale circulation pattern while the ITCZ and SPCZ patterns are unrealistic in some models. Similar to the observational dataset, the spatial distribution of high HLC area in most models is closely linked to the distribution of strong DIV and high SST. Simulations by MPI-ECHAM5, NCAR-CCSM3.0, UKMO-HadCM3 tend to produce most realistic patterns in HLC area as well as DIV and SST. The simulated patterns of HLC area, DIV, and SST of CCCMA-CGCM3.1 are also similar to those of the observation, more similar to SPCZ than to ITCZ. The simulated patterns of HLC area, DIV and SST of MRI-CGCM2.3.2a are similar to those of the observation while HLC area is underestimated. In some models (e.g., GISS-EH, INMCM3.0, NCAR-PCM1), the regions of large DIV and the associated large HLC over the western Pacific stay near 15 N while those in the real ITCZ are found around the equator (Fig. 1). In these models, areas with the large DIV and HLC south of the equator also tend to extend east-west, without exhibiting the northwest-southeast tilt typical of those in the real SPCZ in the observation. In the case of CSIRO3.5, INGV-ECHAM4, IPSL-CM4, MIROC3.2-hires,

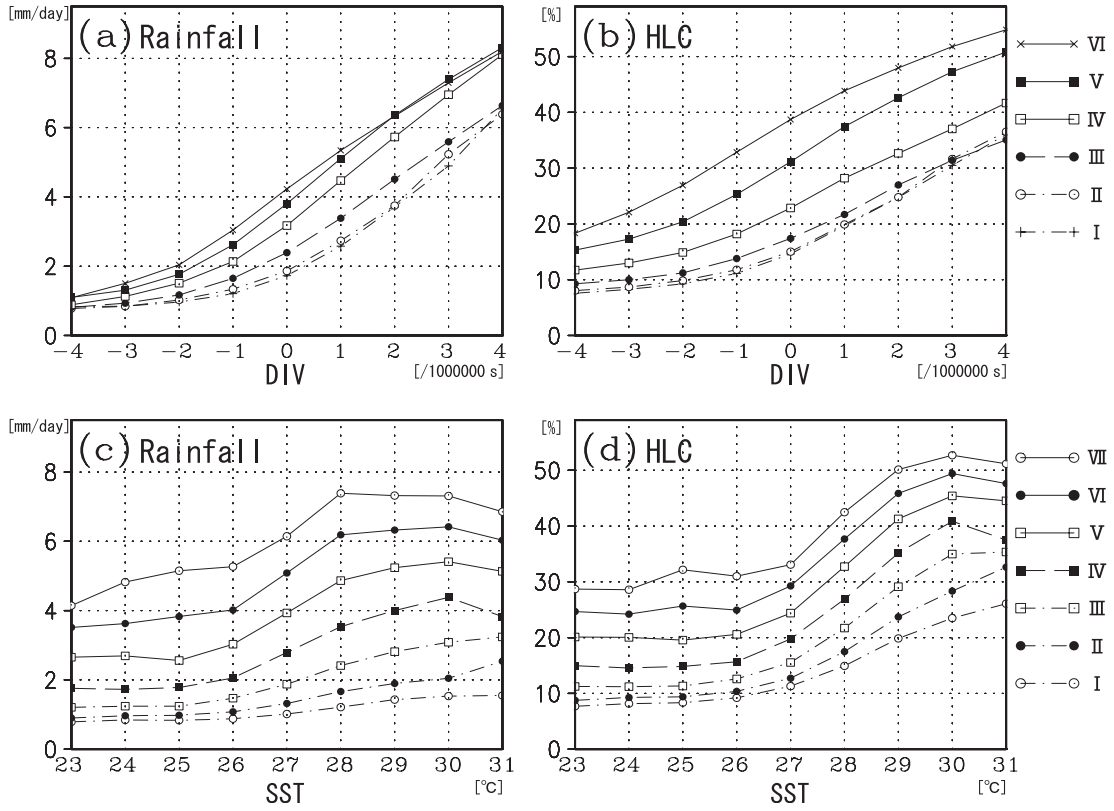

Fig. 3. Observed (a) Rainfall–DIV and (b) HLC–DIV relationships stratified by SST categories (I: 24∼25, II: 25∼26, III: 26∼27, IV: 27∼28, V: 28∼29, VI: 29∼30 [°C]). Observed (C) Rainfall–SST and (d) HLC–SST relationships stratified by DIV categories (I: −3.5∼−2.5, II; −2.5∼−1.5, III: −1.5∼−0.5, IV: −0.5∼0.5, V: 0.5∼1.5, VI: 1.5∼2.5, VII: 2.5∼3.5 [$\times 10^{-6}$ s^{-1}]).

HLC area widely spreads from the Maritime Continent to the Pacific Ocean, and does not show a band-like structure of HLC area reflecting the real ITCZ and SPCZ in spite of the good representation of the DIV field. In particular, in MIROC3.2, a high HLC area spreads extensively owing to the overestimation of HLC[1], especially in medres (not shown). Overall, the inter-model differences in HLC are larger than those in rainfall as analyzed by Dai (2006).

1 MIROC3.2 makes available in PCMDI data base an output of the whole cloud amount ("clt") or cloud area fraction for the whole atmospheric column as seen from the surface or the top of the atmosphere. In MIROC3.2, the fraction of HLC identified by the current maximum overlap assumption method exceeds clt. The overestimation of the HLC in the MIROC3.2 using the maximum overlap assumption method is also indicated in Karlsson et al. (2008). The distribution and absolute amount of clt in MIROC3.2 is much closer to the observation.

b. Relationships of rainfall and HLC with DIV and SST

Both of the large-scale circulation and SST play important roles in the occurrence of tropical rainfall and deeply developed high-level clouds on the climatological mean basis as shown in Fig. 1. The climatological relationships of rainfall and HLC with DIV (SST) as a function of the SST (DIV) are next investigated. Figures 3a and 3b show the observed rainfall–DIV and HLC–DIV relationships, respectively, for different SST categories. The rainfall–DIV and HLC–DIV curves are obtained by computing the mean of rainfall and HLC values at every 1°C SST bin from 24°C to 30°C. As an overall feature, rainfall and HLC increase almost linearly with DIV. Taking a closer look at them, the sensitivities of rainfall and HLC to DIV (i.e., gradient in Figs. 3a, b) are more pronounced in positive DIVs than negative DIVs. An interesting feature is that the sensitivities of rainfall

and HLC to DIV are quite independent of SST while, in general, the magnitude of each parameter at the same DIV is larger for higher SST.

Figures 3c, d show the observed rainfall–SST and HLC–SST relationships, respectively, for the different DIV categories. Both rainfall and HLC do not vary significantly in the range below 26°C, exhibiting a nearly flat distribution, in each category of DIV. On the other hand, it is apparent that each variable is enhanced dramatically around ~27°C. Similar characteristics of other indices for tropical convection as a function of SST have been indicated by previous studies (e.g., Zhang 1993; Waliser and Graham 1993; Masunaga and Kummerow 2006). It should be noted that the abrupt enhancement around 27°C in rainfall and HLC is seen not only in the positive DIVs but also in negative DIVs. In this respect, the relationships of rainfall and HLC with SST are qualitatively similar among different DIV categories. Meanwhile, the sensitivities of rainfall and HLC to SST vary among different DIV categories. The sensitivities of rainfall and HLC to SST from 26–28°C and from 26–29°C, respectively, are higher in the positive DIVs than in the negative DIVs. The sensitivities of rainfall and HLC to SST become weak from 28–30°C and from 29–30°C, respectively, and negative above 30°C in the positive DIVs while they keep almost constantly above 26°C in the negative DIVs. Our result implies that the reduction in rainfall and HLC above 30°C is most pronounced in a small DIV (DIV IV), and does not occur in the negative DIVs. On the other hand, previous studies indicated that the reduction of convection in extreme SSTs (30°C~) may occur in regions of strong subsidence (negative DIVs in this study) forced by convection generated elsewhere, causing a very high SST (Waliser 1996; Lau et al. 1997). The further discussion of this issue of inconsistency between their results and ours is beyond the scope of this paper.

Figure 4 compares the relationships of rainfall and HLC with DIV (Figs. 4a, b) and with SST (Figs. 4c, d) for the observation (a thick solid line) and models (marked thin lines). Figs. 4a, b and Figs. 4c, d are not subdivided by SST and DIV categories, respectively, because the relationships of rainfall and HLC with DIV (SST) are qualitatively similar in that the sensitivities of both variables to DIV (SST) are almost the same among different SST (DIV) categories in the observation. As a general feature, climate models simulate the observed relationships of rainfall and HLC with DIV fairly well (Figs. 4a, b). In the case of rainfall, the relationship of rainfall with DIV is well captured in the models (Fig. 4a). The sensitivity of rainfall to DIV is small in BCCR-BCM2.0 (designated by symbol "*a*" in Fig. 4a) and large in positive DIV in INMCM3.0 ("*k*"), respectively, compared to the observation and other models. In the case of HLC, the sensitivity to DIV in the models is similar to that in the observation, but the magnitude is diverse among the models. The magnitude of HLC is overestimated in MIROC3.2 (both hires "*m*" and medres "*n*"), while it is underestimated in GISS-EH ("*g*"), GISS-ER ("*h*"), and MRI-CGCM2.3.2a ("*p*"). Similar to rainfall, in INMCM3.0 ("*k*"), the sensitivity of HLC to DIV in INMCM3.0 ("*k*") is large for positive DIV. The sensitivity of HLC to DIV in INGV-ECHAM4 ("*j*") is relatively small through all DIVs.

Compared to the reasonable agreement in the relationships of rainfall and HLC with DIV, the relationships of rainfall and HLC with SST exhibit larger differences among the models (Figs. 4c, d). Most models capture the sudden enhancement in rainfall around the threshold value at 27–28°C. However, the rainfall amount tends to be overestimated, particularly above ~27–28°C, accompanied by high sensitivity of rainfall to SST compared to the observation. The sensitivity of rainfall to SST above 30°C is almost constant in some models [CSIRO3.5 ("*d*"), GFDL-CM2.0 ("*e*"), IAP-FGOALS-g1.0 ("*i*"), NCAR-PCM1 ("*r*"), UKMO-HadCM3 ("*s*")]. Abrupt enhancement in rainfall occurs at a lower SST in BCCR-BCM2.0 ("*a*"), INMCM3.0 ("*k*"), and Miroc3.2-medres ("*n*"). Compared to rainfall, HLC behaves differently from a model to another in both sensitivity to SST and magnitude. Most models underestimate the sensitivity to SST around 27°C. The unrealistic representation in the relationship of HLC with SST would be related to the model deficiency to simulate ice cloud amount as was pointed out by Su et al. (2006b). CCCMA-CGCM3.1 ("*b*", "*c*"), MPI-ECHAM5 ("*o*") and NCAR-CCSM3.0 ("*q*") exhibit results similar to the observation.

3.2 Spatial relationships of rainfall and HLC areas with DIV associated with subseasonal disturbances over ITCZ

In the previous section, it is confirmed that the general relationships of rainfall and HLC with DIV as an index of large-scale circulation are well

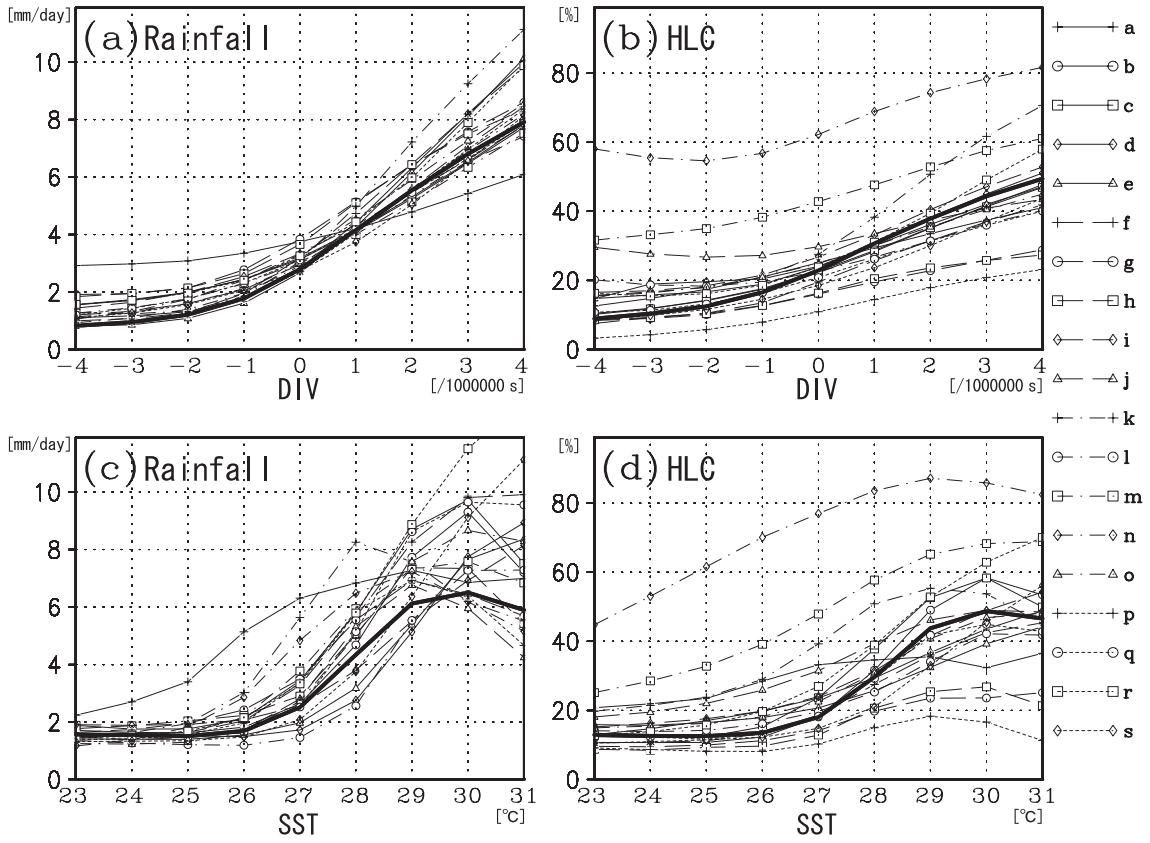

Fig. 4. Comparison of the observation (a thick solid line) and AOGCMs (marked thin lines: alphabets at right legend indicate each model as labeled in Table 1) for (a) Rainfall–DIV and (b) HLC–DIV, and for (c) Rainfall–SST and (d) HLC–SST relationships.

captured in the AOGCMs as shown in Figs. 4a, b; the sensitivities of rainfall and HLC to DIV are well captured in the models. The result encourages further analyses for the models. In this section, the spatial relationships of rainfall and HLC areas with DIV associated with subseasonal disturbances are analyzed for ITCZ through a composite analysis. The composite analysis is focused on the western and central Pacific where the dominant rainfall and HLC band appear in each model (rainfall and HLC areas over the eastern Pacific tend to be faint in some models; see Fig. 2 in this study and also Fig. 1 in Dai 2006).

a. Method of composite analysis

The spatial patterns of rainfall and HLC areas around the DIV centers associated with subseasonal disturbances over ITCZ are investigated through a composite analysis. OLR is also included for the present analysis as an index for deep convection. Convective activity and the associated rainfall and HLC are tied not only to subseasonal large-scale circulation but also to slowly varying environmental conditions including the underlying SST pattern. We try to isolate the impact of large-scale circulation associated with subseasonal disturbances on rainfall, HLC, and OLR from that of the slowly varying environmental conditions. To exclude such environmental conditions, the seasonal cycle is firstly removed by subtracting monthly climatologies from monthly mean data for each variable to yield monthly anomalies, which are used for the composite analysis. In addition, months corresponding to El Nino and La Nina phases that accompany ENSO are excluded from the composite. The both phases are determined by the definition used in Vecchi and Harrison (2004) where periods corresponding to monthly anomalies of NINO.3 (150 W–90 W, 5 S–5 N) SST above 0.75°C and below −0.75°C are identified as El Nino and La

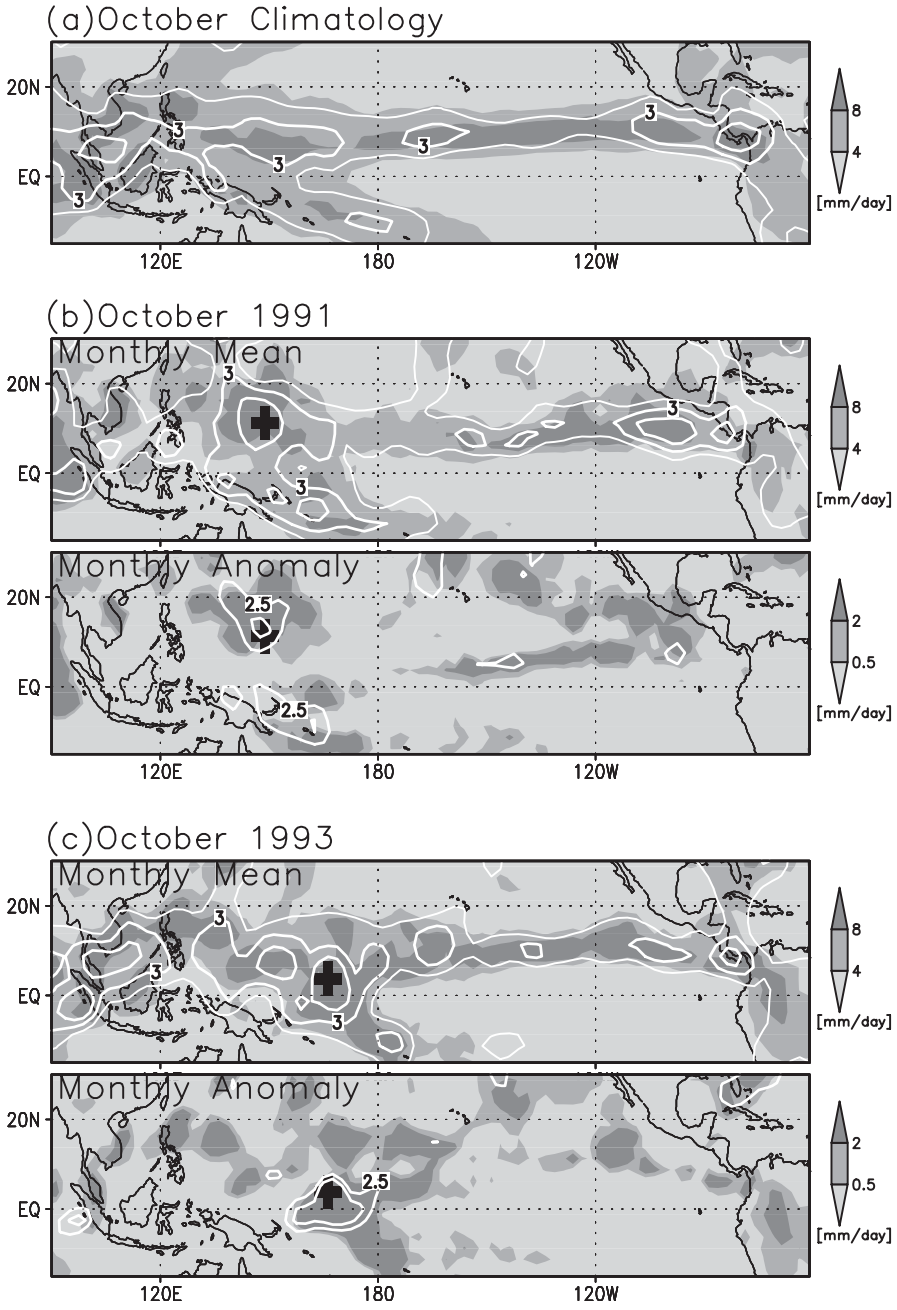

Fig. 5. Spatial distributions of DIV (white solid contours) and Rainfall (grey scale) in October for (a) climatology (1984–1999), and those for monthly mean and monthly anomaly from monthly climatology in (b) 1991 and (c) 1993. DIV at 1.0, 3.0, 5.0 [$\times 10^{-6}$ s^{-1}] are contoured for climatology and monthly mean, and DIV at 2.5, 4.0 [$\times 10^{-6}$ s^{-1}] are contoured for monthly anomaly. A DIV center is plotted by a black crossed mark in (b) and (c).

Nina phases, respectively. El Nino and La Nina phases are determined for the observation and for each model individually.

More specifically, the composite technique is applied as follows. At first, a geographical center of DIV for raw monthly mean data is sought for every month during 1984–1999 except El Nino and La Nina phases in area domains containing cli-

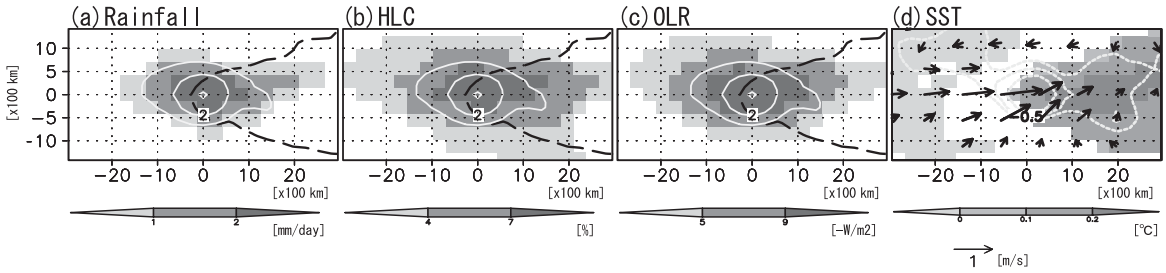

Fig. 6. Spatial distribution of (a) Rainfall, (b) HLC, and (c) OLR (grey scale) composited around the DIV center over the western and central Pacific. DIV at 0.75, 2, 4 [$\times 10^{-6}$ s^{-1}] (white solid contours) and SST at 0.1 [°C] (a black dashed contour) are superposed. (d) Detailed SST pattern (grey scale), and horizontal wind (vector) and convergence (grey dotted contours; −1, −0.5, −0.25 [$\times 10^{-6}$ s^{-1}]) at 1000 hPa. X and Y axes indicate the relative distances from the DIV center of eastward and northward, respectively. Portions with statistically significance exceeding the 95% confidential level are only described. See the text about the composite technique for detail.

matological ITCZ over the western and central Pacific (140 E–120 W, 1.25 S–12.5 N). Once the DIV center is detected, monthly anomalies for rainfall, HLC, and OLR as well as DIV are composed against the horizontal location of the DIV center.

b. Spatial pattern in the observation

The spatial patterns of DIV (white solid contours) and rainfall (in grey scale) areas in October for climatology are shown in Fig. 5a, and those for the monthly mean and monthly anomaly in 1991 and 1993 are shown in Figs. 5b and c, respectively, as examples. The horizontal position of the DIV center over the western and central Pacific is plotted by a thick cross ('+') in Figs. 5b, c. The horizontal position of the DIV center for each year does not stay at a fixed position but varies from a year to another. DIV and rainfall patterns also vary from a year to another around the DIV center. When the monthly climatology as a background mean field is subtracted, DIV and rainfall patterns are found to be spatially confined around the DIV center in the monthly anomaly field. We compose the monthly anomaly field with respect to the DIV center, representing a subseasonal disturbance, for each year, and investigate the mean spatial pattern of subseasonal disturbances shown in composite anomalies. As such, the dynamical linkage of rainfall and HLC areas with subseasonal large-scale circulation can be investigated with a year-to-year variability of the DIV center properly taken into account.

The results of the composite analysis for rainfall, HLC, and OLR anomalies are shown in Figs. 6a, b, c (in grey scale). The anomalies of DIV (white solid contours) and SST (a black dashed contour) are also plotted. The positive DIV anomaly has its maximum over the center of DIV, corresponding to the maximum location in the distribution of the raw DIV in each month, and spreads around the center with stretching more zonally, i.e., more to east-west than north-south. The spatial distribution of each variable (rainfall, HLC, and OLR) spreads more zonally in a manner similar to the DIV. It is noted that highly positive anomalies of the variables spread more to the eastern part of the DIV center than to the western part. This might be associated with a positive SST anomaly spreading to the east of the DIV center, particularly with a highly positive anomaly nearly along at 0° in the reference latitude (0 km in the vertical axis of Fig. 6). To the west of the DIV center, a negative SST anomaly spreads from the DIV center. At a low-level (1000 hPa), the wind anomaly pattern shown by Fig. 6d is presumably related to the atmospheric response to the heat source due to the convection located north of the equator within ITCZ (Hecky and Gill 1984) where the DIV centers are identified through all the period of this analysis. The resultant pattern in a low-level wind anomaly might be linked to the SST anomaly pattern. To the east of the DIV center, a westerly anomaly becomes weaken near the reference latitude of 0° to which a wind anomaly tends to converge from both north and south. To the west of the DIV center, counter-clockwise and clockwise turns of wind anomalies are seen at north and south of the DIV center, respectively.

Table 2. Zonal width [×100 km] of Rainfall, HLC, and OLR around the DIV center identified in the western and central Pacific in the observation.

Rainfall	HLC	OLR
9.39	10.70	10.23

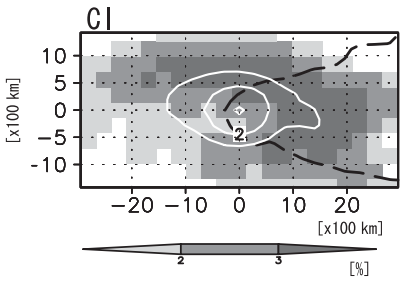

Fig. 7. Same as Fig. 6b, but for CI.

c. *Zonal widths of horizontal pattern of rainfall, HLC, OLR, and DIV* areas *in the observation*

In order to evaluate the zonally extended feature quantitatively, the "zonal width" is defined here. First, zonal distribution of each variable averaged meridionally between ±400 km from the DIV center is obtained. Then, the standard deviation of the composite anomalies at the zonal distance from the DIV center is calculated within ±2000 km zonal distance from the DIV center. The resultant standard deviation of zonal distance of each variable is defined as the zonal width. Interestingly, the zonal width varies from a variable to another as shown in Table 2. The zonal width of HLC area is the largest (1070 km), followed by that of OLR (1023 km). Compared to HLC and OLR areas, the zonal width of the rainfall area (939 km) is somewhat narrower. The difference of the zonal width among the variables is compared with that of each type of high clouds, i.e., DC, CS, and CI, as mentioned below. Figure 7 shows the composite map of CI area around the DIV center. It is apparent that CI area exhibits a more widespread distribution than rainfall, HLC, and OLR areas around the DIV center, particularly to the east of DIV center. Compared to this particular pattern in CI area, the spatial pattern of DC and CS areas in the composite (not shown) is quite similar to that of the rainfall area. As shown in Table 3, the zonal width of CI area (1184 km) is larger than any other variable while the widths of DC (937 km) and CS (976 km) areas are smaller than those of HLC and OLR areas. The zonal width of DC area is close to that of the rainfall area. The broad zonal width of HLC area, a characteristic in Table 2, is thus due largely to CI area.

Table 3. Same as Table 2, but for each cloud type of DC, CS, CI.

DC	CS	CI
9.37	9.76	11.84

d. *Evaluation of the zonal widths in the models*

In order to evaluate the patterns of rainfall, HLC, OLR, and DIV anomalies along ITCZ in the models, the same composite analysis as applied to the observation is applied to the outputs of the models to calculate the zonal widths. Figure 8 shows the inter-model comparison of the zonal width of each variable as well as the observation (a: DIV, b: rainfall, c: HLC, d: OLR). The horizontal axis in each figure shows the temporal correlation between rainfall and DIV at the DIV center which is derived from the time sequence of monthly anomaly data except El Nino and La Nina phases in each model. Because the rainfall amount is strongly related to the column integrated latent heating, the correlation between rainfall and DIV at the DIV center indicates the degree of relationship of the large-scale circulation field with the column integrated latent heating consisting mainly of the aggregation of cumulus latent heating. The large correlation means that the latent heating strongly influences subseasonal large-scale circulation by enhancing the upward motion through the atmospheric warming, potentially leading to upper-level divergence at the DIV center. The large-scale circulation may in turn induce low-level convergence to help trigger the convection. A most prominent feature in Fig. 8 is the systematic model bias that the zonal width is underestimated in all variables compared to the observation (a filled circle) with a few exceptions that are particularly seen in the rainfall area. The zonal widths of models reproduce those of the observation better in the rainfall area than in HLC area. The zonal widths of HLC area in the models tend to be close to those of the rainfall area or even smaller in some models while the zonal width of HLC area is larger than that of the rainfall area in the observation.

It is noted that, in the models, the zonal width

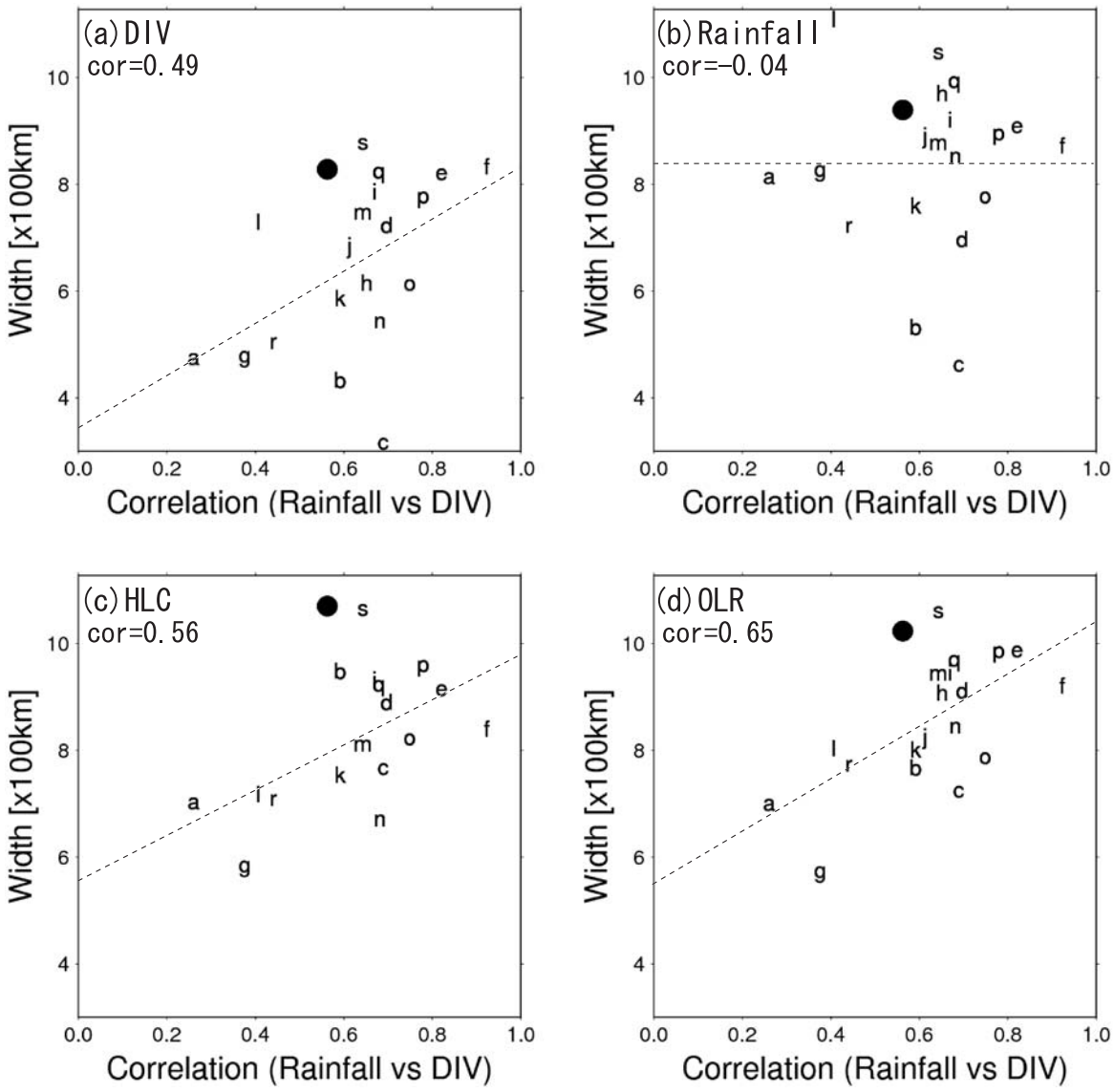

Fig. 8. Scatter plots of zonal width of (a) DIV, (b) Rainfall, (c) HLC, and (d) OLR against correlation between rainfall and DIV at the DIV center over the western and central Pacific on the basis of the composite for the observation (a filled circle) and for 19 AOGCMs (alphabets; each model as labeled in Table 1). Inter-model correlations (cor) are indicated at the upper left in each panel. A regressed slope among the models is described by a dotted line for each panel. Plots of GISS-ER and INGV-ECHM4 are omitted in (c) HLC because significant positive anomalies cannot be seen around the DIV center.

of DIV area (Y-axis) increases with the correlation between rainfall and DIV (X-axis) in Fig. 8a. The inter-model correlation of the rainfall-DIV relationship and the zonal width of DIV area is 0.49, exceeding the 95% confidence level. As is described above, the stronger correlation between rainfall and DIV at the DIV center implies that subseasonal large-scale circulation interacts more closely with cumulus latent heating. Figure 8a, thus, indicates that a model with a tighter coupling of the subseasonal large-scale circulation field with the cumulus latent heating tends to have a wider spread of DIV area around the DIV center. Similar inter-model positive correlations between the zonal width (Y-axis) and rainfall-DIV relationship (X-axis) can be also seen in HLC (Fig. 8c) and OLR (Fig. 8d)

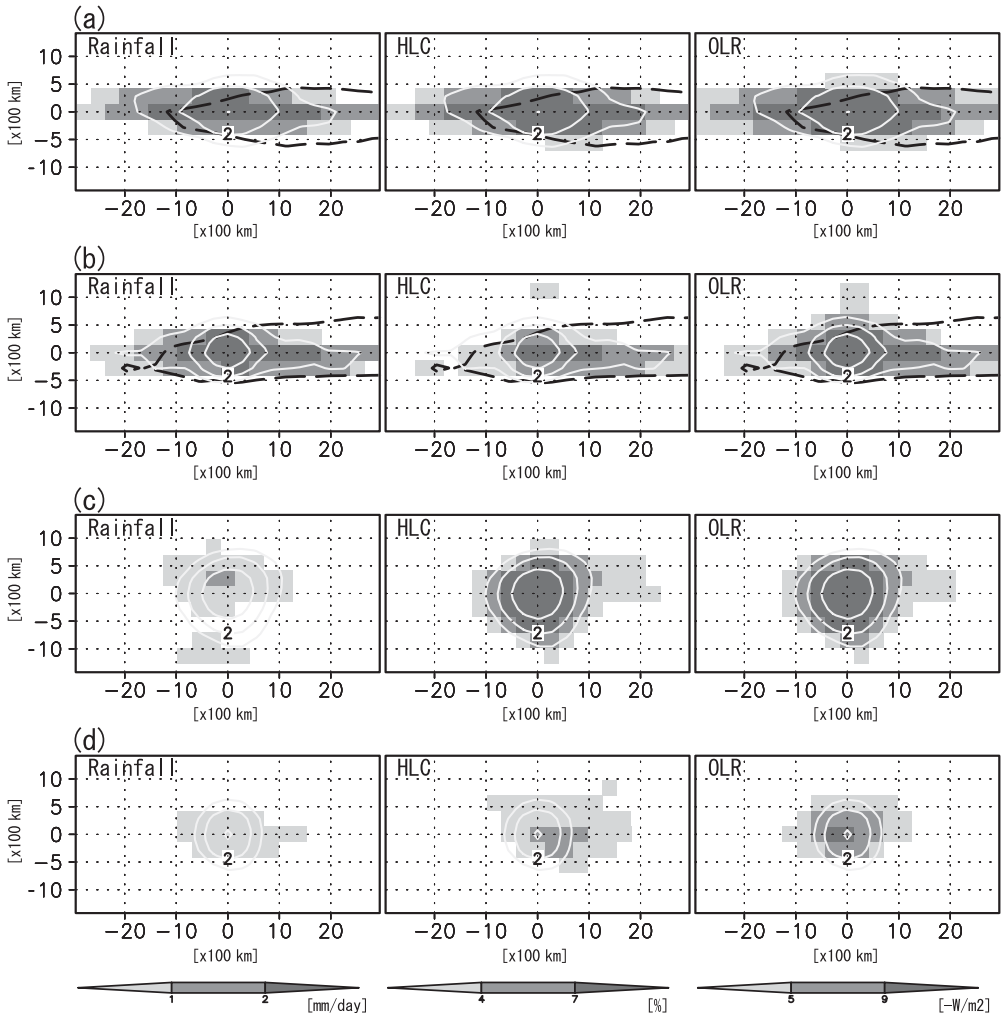

Fig. 9. Same as Fig. 6a, b, c, but for each climate model (a: UKMO-HadCM3, b: NCAR-CCSM3.0, c: BCCR-BCM2.0, d: CCCMA-CGCM3.1-t63).

areas. Figures 8a, c, d show that a model better reproducing the zonal width of DIV, HLC, and OLR areas tends to have stronger coupling of the large-scale circulation field with the cumulus latent heating than the observation. In the case of rainfall (Fig. 8b), the zonal width does not strongly depend on the correlation between rainfall and DIV. In Fig. 8, the reproducibility of the zonal width in each variable has no clear relation to the horizontal resolutions and convection schemes that are used in each model.

Figure 9 shows the composite spatial pattern of each variable in the anomaly around the DIV center for two pairs of models showing the contrast of the performances of DIV (Fig. 8a). Pair A shown by Figs. 9a, b is the two models of UKMO-HadCM3 ("*s*" in Fig. 8) and NCAR-CCSM3.0 ("*q*") that are very close to the observation in Fig. 8a while Pair B shown by Figs. 9c, d is BCCR-BCM2.0 ("*a*") and CCCMA-CGCM3.1-t63 ("*c*") that are far from the observation in Fig. 8a. The composite three variables of rainfall, HLC, and OLR as well as DIV at the DIV center in Pair A (Figs. 9a, b) exhibit a zonally wide spread distribution, close to those of the observation (Figs. 6a, b, c), while they exhibit a meridionally narrower distribution than the observation. Their strengths of anomalies of rainfall, HLC, and OLR at the DIV center are also close to those of the observation (Figs. 6a, b, c). It should be noticed that Pair A reproduces well the observed SST anomaly distribution in the composite. In contrast to Pair A, the

composite three variables as well as DIV in Pair B (Figs. 9c, d) tend to be significantly more concentrated around the DIV center than those of the observation (Figs. 6a, b, c). The strength of positive anomalies at the DIV center is underestimated for rainfall (rainfall, HLC, and OLR) in BCCR-BCM2.0 (CCCMA-CGCM3.1-t63) of Pair B. In addition, Pair B does not reproduce the observed SST anomaly distribution. BCCR-BCM2.0 and CCCMA-CGCM3.1-t63 of Pair B exhibit negative and small positive anomalies of SST, respectively, at the DIV center (the negative and small positive value contours, respectively, do not appear in Figs. 9c, d because they are out of range of the selected contours that are the same as those of the observation shown in Fig. 6).

3.3 Reproducibility of the climatological mean field and that of subseasonal disturbances in the models

In this section, we compare the reproducibility of the simulated climatological mean field described in Section *3.1* and that of the composite anomalies, which represent subseasonal disturbances, in the monthly mean field described in Section *3.2*.

The model's performance of the horizontal spread in the composite analysis in Section *3.2* is closely related to its capability of simulating the observed climatological mean pattern of DIV and HLC areas over ITCZ in Section *3.1*. For example, UKMO-HadCM3 and NCAR-CCSM3.0 of Pair A, which produce a realistic composite pattern, well simulate the climatological mean pattern of DIV and HLC areas along the location of the observed ITCZ (Figs. 1d, 2) while NCAR-CCSM3.0 tends to slightly underestimate HLC amount over the western Pacific as shown by Fig. 2. In addition to these two models of Pair A, the models the positions of which for variables studied (DIV, rainfall, HLC) in Fig. 8 locate relatively close, depending on variables, to the observation, e.g., IAP-FGOALS-g1.0 ("*i*"), MIROC3.2-hires ("*m*"), and MRI-CGCM2.3.2a ("*p*") indeed capture well the climatological mean ITCZ pattern as is shown by Fig. 2 or Dai (2006).

In BCCR-BCM2.0 of Pair B, where the negative SST anomaly appears around the DIV center in the composite analysis, DIV is not linked to SST in a proper manner in the climatolotical mean pattern as shown in Fig. 2. In the case of CCCMA-CGCM3.1 of Pair B, where the distribution of DIV and HLC areas is too much concentrated around the DIV center in the composite analysis, the area with large DIV and HLC in the climatological mean pattern is confined to the western Pacific west of 180 E and ITCZ is faint along the location of the observed ITCZ as shown in Fig. 2.

Some of other models are briefly referred to as follows. In GISS-ER and INGV-ECHAM4, whose marks are not plotted in Fig. 8c because the significant HLC anomaly is not seen in the composite plane around the DIV center, HLC area is not linked to DIV in a proper manner in the climatological mean pattern. In GISS-EH ("*g*"), which exhibits a relatively smaller zonal width (Fig. 8), the location of large DIV over ITCZ in the climatological mean pattern is completely different from that of the observation in the way that it is too far north of the equator in latitude and too far east around the central-eastern Pacific in longitude (Fig. 2).

4. Summary and discussion

In this study, relationships of rainfall and high-level cloud areas with large-scale circulation over the tropical Pacific Ocean in the latest generation AOGCMs were evaluated. As an overall feature, most models well represent the observed climatological relationships of rainfall and HLC areas with large-scale circulation. In order to evaluate the horizontal relationships of rainfall and high-level cloud areas with large-scale circulation associated with subseasonal disturbances over the tropical Pacific Ocean, the distribution of rainfall, HLC, and OLR is composed around the DIV center along ITCZ, using DIV as an index of large-scale circulation. Monthly anomalies against monthly climatologies are used for the composite except El Nino and La Nina phases. The composite analysis turned out to be useful for studying the horizontal relationships of rainfall, HLC, and OLR areas around the DIV centers associated with subseasonal disturbances over ITCZ.

Figure 10 schematically illustrates the result of the analysis. A comparison between AOGCMs and observations reveals that, as one of the systematic model biases, the subseasonal large-scale circulation field and the related rainfall, HLC, and OLR are underestimated for the spread, i.e., more localized around the ascent region in most of the models than in the observation. Particularly, the horizontal spread of HLC area is largely underestimated by the models. The spread tends to be less different between rainfall and HLC areas in the models than in

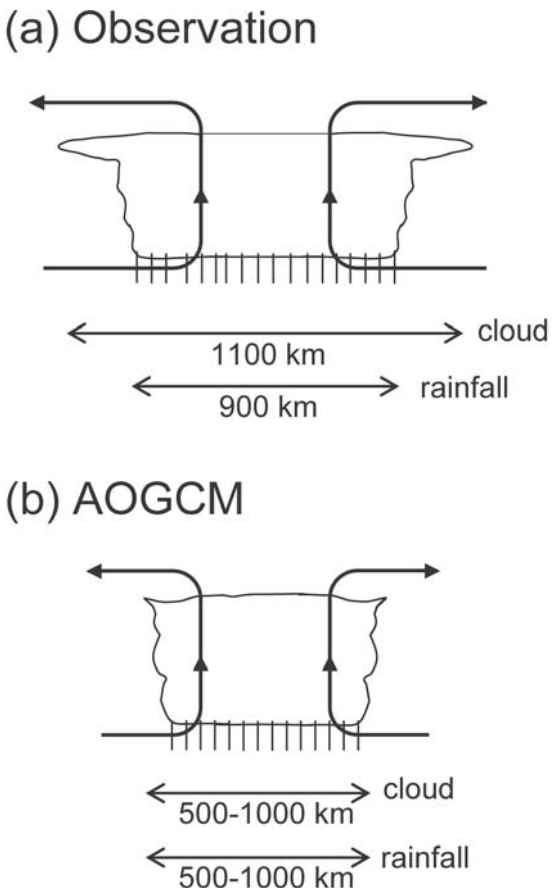

Fig. 10. Schematics of large-scale circulation field and cloud/rainfall associated with subseasonal disturbances (see the last paragraph but one of Section 1) along the east-west direction in the (a) observation and (b) AOGCM.

the observation. HLC area spreads more extensively than the rainfall area in the observation owing to the widespread high-level cirrus clouds, suggesting that the physical processes relevant to the spatial distribution of HLC area cannot be captured well in the models.

The large-scale circulation field and related HLC and OLR areas spread more widely in the models that exhibit a strong coupling between the large-scale circulation and the cumulus latent heating. The result would be presumably explained by the positive feedback that the cumulus latent heating enhances the large-scale upward motion leading to the spread of upper-level divergence, which strengthens the large-scale circulation motion that induces the enhanced low-level convergence leading to the enhanced cumulus convection. On the other hand, the coupling in the models that reproduce the observed spread of HLC and OLR areas tends to be too strong.

The model's performance of the horizontal spread in the composite anomalies is closely related to its capability of simulating the observed climatological mean pattern of each variable. A model well reproducing the observed spread of each variable around the DIV center tends to well simulate the climatological mean pattern of each variable over ITCZ.

It is interesting to see if the spread of each variable around the DIV center can be associated with model specifications such as the spatial resolutions and convection schemes. Broadly speaking, the reproducibility of the spread appears not to exhibit a systematic dependence on the spatial resolutions and convection schemes that are used in each model. Probably, we must also consider the dependence not only on the convection schemes but also on the large-scale condensation clouds schemes. Nevertheless, certain dependence on convection schemes might be suggested from the results of this study. Considering the fact that the large-scale circulation and the related HLC and OLR areas spread widely in the models where large-scale circulation is tightly coupled to the cumulus latent heating, the spread could be wide in the models requiring the quasi-equilibrium state between large-scale forcing and convection as is assumed in the Arawawa-Schubert scheme. That is particularly true of GFDL-CM2.0 ("*e*"), GFDL-CM2.1 ("*f*"), and MRI-CGCM2.3.2 ("*p*") adopting the Arakawa-Schubert scheme as is shown in Figs. 8a, c, and d while the spread of HLC and OLR areas in GFDL-CM2.1 is rather small compared to those in the other two models. For these models, however, the coupling between large-scale circulation and cumulus latent heating is too strong compared to the observation while the spread is close to the observation. In the case of MIROC3.2-hires ("*m*") and MIROC3.2-medres ("*n*"), adopting the Arakawa-Schubert scheme but applying convection suppression modification using a threshold of relative humidity (Emori et al. 2001), the coupling is close to the observation while the spread is small compared to the observation. It should be noted that the spread of each variable is wider and nearer to the observation in MIROC3.2-hires ("*m*") than in MIROC3.2-medres ("*n*"), i.e., in the higher spatial resolution model. In contrast

to the model using the quasi-equilibrium assumption, the model using the assumption of a strong dependence of convection on relative humidity as BCCR-BCM2.0 ("*a*") is weaker in the coupling and smaller in the spread in the models; it is also weaker and smaller than the observation.

Overall, the underestimation of the spread of the high-level cloud area in AOGCMs is obvious in our result, suggesting the systematic bias in the representation of anvil cirrus clouds in AOGCMs. Luo and Rossow (2004) indicated that tropical cirrus can advect over large distance, about 600–1000 km, during its lifetime in association with large-scale lifting as the replenishing process to maintain the cirrus much longer than the particle lifetime. Because the distance spans more than one grid box in current AOGCMs, they suggested that the advection term needs to be properly designed for the water vapor and cloud water budget in AOGCMs. An implementation of such a process would be of great advantage for the improvement of the current skill of representing clouds and rainfall in AOGCMs.

Acknowledgments

We acknowledge the modeling groups, the Program for Climate Model Diagnosis and Intercomparison (PCMDI), and the World Climate Research Programme's (WCRP's) Working Group on Coupled Modelling (WGCM) for their roles in making available the WCRP Coupled Model Intercomparison Project phase 3 (CMIP3) multi-model dataset. Support of this dataset is provided by the Office of Science, U. S. Department of Energy. The climatological monthly mean ISCCP D2 data are obtained from the NASA Langley Research Center Atmospheric Science Data Center. This research was supported by the Global Environment Research Fund (S-5-2) of the Ministry of the Environment, Japan, and by the "Data Integration and Analysis System" Fund for National Key Technology from the Ministry of Education, Culture, Sports, Science and Technology, Japan.

References

Arakawa, A., and W. H. Schubert, 1974: Interaction of a cumulus cloud ensemble with the large-scale environment, Part I. *J. Atmos. Sci.*, **31**, 674–701.

Adler, R. F., and Coauthors, 2003: The version-2 Global Precipitation Climatology Project (GPCP) monthly precipitation analysis (1979–present). *J. Hydrometeor.*, **4**, 1147–1167.

Back, L. E., and C. S. Bretherton, 2008: Geographic variability in the export of moist static energy and vertical motion profiles in the tropical Pacific. *Geophys. Res. Lett.*, **33**, L17810, doi:10.1029/2006GL026672.

Berg, W., C. Kummerow, and C. A. Morales, 2002: Differences between east and west Pacific rainfall systems. *J. Climate*, **15**, 3659–3672.

Bony, S., J. -L. Dufresne, H. Le Treut, J. -J. Morcrette, and C. Senior, 2004: On dynamic and thermodynamic components of cloud changes. *Climate Dyn.*, **22**, 71–86.

Collins, W. D., and Coauthors, 2006: The Community Climate System Model: CCSM3. *J. Climate*, **19**, 2122–2143.

Dai, A., 2006: Precipitation characteristics in eighteen coupled climate models. *J. Climate*, **19**, 4605–4630.

Del Genio, A. D., and W. Kovari, 2002: Climatic properties of tropical precipitating convection under varying environmental conditions. *J. Climate*, **15**, 2597–2615.

Delworth, T. L., and Coauthors, 2006: GFDL's CM2 global coupled climate models. Part 1: Formulation and simulation characteristics. *J. Climate*, **19**, 643–674.

Deque, M., C. Dreveton, A. Braun, and D. Cariolle, 1994: The ARPEGE/IFS atmospheric model: A contribution to the French community climate modeling. *Climate Dyn.*, **10**, 249–266.

Diansky, N. A., and E. M. Volodin, 2002: Simulation of present-day climate with a coupled atmosphere-ocean general circulation model (English translation). *Izv. Atmos. Ocean. Phys.*, **38**, 732–747.

Emori, S., T. Nozawa, A. Numaguti, and I. Uno, 2001: Importance of cumulus parameterization for precipitation simulation over East Asia in June. *J. Meteor. Soc. Japan*, **79**, 939–947.

Flato, G. M., G. J. Bore, W. G. Lee, N. A. McFarlane, D. Ramsden, M. C. Reader, and A. J. Weaver, 2000: The Canadian Centre for Climate Modelling and Analysis Global Coupled Model and its climate. *Climate Dyn.*, **16**, 451–467.

Gordon, C., C. Cooper, C. A. Senior, H. T. Bankds, J. M. Gregory, T. C. Johns, J. F. B. Mitchell, and R. A. Wood, 2000: The simulation of SST, sea ice extents and ocean heat transports in a version of the Hadley Centre coupled model without flux adjustments. *Climate Dyn.*, **16**, 147–168.

Gordon, H. B., and Coauthors, 2002: The CISRO Mk3 Climate System Model. CISRO Atmospheric Research Tech. Paper 60, 130 pp. [Available online at http://www.dar.csiro.au/publications/gordon_2002a.pdf.]

Gualdi, S., E. Scoccimarro, A. Bellucci, A. Grezio, E. Manzini, and A. Navarra, 2006: The main feature of the 20th Century climate as simulated with SXG coupled GCM. Claris Newsletter issue 4.

Hartmann, D. L., L. A. Moy, and Q. Fu, 2001: Tropical convection and the energy balance at the top of the atmosphere. *J. Climate*, **14**, 4495–4511.

IPCC, 2007: Climate Change 2007: The Physical Science Basis. Contribution of Working Group I to the Fourth Assessment Report of the Intergovermental Panel on Climate Change. Solomon, S., D. Qin, M. Manning, Z. Chen, M. Marquis, K. B. Averyt, M. M. Tignor, H. L. Miller (eds.). Cambridge University Press, Cambridge, 996 pp.

Heckley, W. A., and A. E. Gill, 1984: Some simple analytical solutions to the problem of forced equatorial long waves. *Quart. J. Roy. Meteor. Soc.*, **110**, 203–217.

Karlsson, J., G. Svensson, and H. Rodhe, 2008: Cloud radiative forcing of subtropical low level clouds in global models. *Climate Dyn.*, **30**, 779–788.

Klein, S., and C. Jakob, 1999: Validation and sensitivities of frontal clouds simulated by ECMWF model. *Mon. Wea. Rev.*, **127**, 2514–2531.

Kubar, T. L., D. L. Hartmann, and R. Wood, 2007: Radiative and convective driving of tropical high clouds. *J. Climate*, **20**, 5510–5526.

K-1 Model Developers, 2004: K-1 coupled model (MIROC) description. H. Hasumi and S. Emori (eds.), K-1 technical report 1, Center for Climate System Research, University of Tokyo, 23 pp.

Lau, K. -M., H. -T. Wu, and S. Bony, 1997: The role of large-scale atmospheric circulation in the relationship between tropical convection and sea surface temperature. *J. Climate*, **10**, 381–392.

Liebmann, B., and C. A. Smith, 1996: Description of a complete (interpolated) outgoing longwave radiation dataset. *Bull. Amer. Meteor. Soc.*, **77**, 1275–1277.

Lindzen, R. S., and S. Nigam, 1987: On the role of sea surface temperature gradients in forcing low-level winds and convergence in the tropics. *J. Atmos. Sci.*, **44**, 2418–2436.

Luo, Z., and W. B. Rossow, 2004: Characterizing tropical cirrus life cycle, evolution, and interaction with upper-tropospheric water vapor using Lagrangian trajectory analysis of satellite observations. *J. Climate*, **17**, 4541–4563.

Marti, O., and Coauthors, 2005: The new IPSL climate system model: IPSL-CM4. Institut Pierre Simon Laplace Tech. Note 26, 84 pp. [Available online at http://dods.ipsl.jussieu.fr/omamce/IPSLCM4/DocIPSLCM4/FILES/DocIPSLCM4_color.pdf.]

Masunaga, H., T. S. L'Ecuyer, and C. D. Kummerow, 2005: Variability in the characteristics of precipitation systems in the tropical Pacific. Part I: Spatial structure. *J. Climate*, **18**, 823–840.

Masunaga, H., and C. D. Kummerow, 2006: Observations of tropical precipitating clouds ranging from shallow to deep convective systems. *Geophys. Res. Lett.*, **33**, L16805, doi:10.1029/2006GL026547.

Reynolds, R. W., and T. M. Smith, 1994: Improved global sea surface temperature analysis using optimum interpolation. *J. Climate*, **7**, 929–948.

Roeckner, E., and Coauthors, 2003: The atmospheric general circulation model ECHAM5. Part I: Model description. Max Planck Institute for Meteorology Rep. 349, 127 pp.

Rossow, W. B., and R. A. Schiffer, 1999: Advances in understanding clouds from ISCCP. *Bull. Amer. Meteor. Soc.*, **80**, 2261–2287.

Schmidt, G. A., and Coauthors, 2006: Present day atmospheric simulations using GISS ModelE: Comparison to in situ, satellite and relanalysis data. *J. Climate*, **19**, 153–192.

Stephens, G. L., 2005: Cloud feedbacks in the climate system: A critical review. *J. Climate*, **18**, 237–273.

Su, H., W. G. Read, J. H. Jiang, J. W. Waters, D. L. Wu, and E. J. Fetzer, 2006a: Enhanced positive water vapor feedbacks associated with tropical deep convection: New evidence from Aura MLS. *Geophys. Res. Lett.*, **33**, L05709, doi:10.1029/2005GL025505.

Su, H., D. E. Waliser, J. H. Jiang, J. -L. Li, W. G. Read, J. W. Waters, and A. M. Tompkins, 2006b: Relationship of upper tropospheric water vapor, clouds and SST: MLS observations, ECMWF analyses and GCM simulations. *Geophys. Res. Lett.*, **33**, L22802, doi:10.1029/2006GL027582.

Uppala, S. M., and Coauthors, 2005: The ERA-40 reanalysis. *Quart. J. Roy. Meteor. Soc.*, **131**, 2691–3012.

Vecchi, G. A., and D. E. Harrison, 2000: Tropical Pacific sea surface temperature anomalies, El Nino, and Equatorial westerly wind events. *J. Climate*, **13**, 1814–1830.

Waliser, D. E., and N. E. Graham, 1993: Convective cloud systems and warm pool sea surface temperatures: Coupled interactions and self-regulation. *J. Geophys. Res.*, **98**, 12881–12893.

Waliser, D. E., 1996: Formation and limiting mechanisms for very high sea surface temperature: Linking dynamics and thermodynamics. *J. Climate*, **9**, 161–188.

Washington, W. M., and Coauthors, 2000: Parallel climate model (PCM) control and transient simulations. *Climate Dyn.*, **16**, 755–774.

Weare, B. C., 2004: A comparison of AMIP II model cloud layer properties with ISCCP D2 estimates. *Climate Dyn.*, **22**, 281–292.

Webb, M., C. Senior, S. Bony, and J. Morcrette, 2001: Combining ERBE and ISCCP data to assess clouds in the Hadley Centre, ECMWF and LMD atmospheric climate models. *Climate Dyn.*, **17**, 905–922.

Williams, K. D., and G. Tselioudis, 2007: GCM intercomparison of global cloud regimes: Present-day

evaluation and climate change response. *Climate Dyn.*, **29**, 231–250.

Wyant, M. C., C. S. Bretherton, J. T. Bacmeister, J. T. Kiehl, I. M. Held, M. Zhao, S. A. Klein, and B. J. Soden, 2006: A comparison of low-latitude cloud properties and their response to climate change in three AGCMs sorted into regimes using mid-troposphere vertical velocity. *Climate Dyn.*, **27**, 261–279.

Yanai, M., and T. Tomita, 1998: Seasonal and interannual variability of atmospheric heat sources and moisture sinks as determined from NCEP-NCAR Reanalysis. *J. Climate*, **11**, 463–482.

Yu, Y., X. Zhang, and Y. Guo, 2004: Global coupled ocean-atmosphere general circulation models in LASG/IAP. *Adv. Atmos. Sci.*, **33**, 976–991.

Yukimoto, S., and Coauthors, 2006: Present-day climate and climate sensitivity in the Meteorological Research Institute Coupled GCM, Version 2.3 (MRI-CGCM2.3). *J. Meteor. Soc. Japan*, **84**, 333–363.

Zhang, C., 1993: Large-scale variability of atmospheric deep convection in relation to sea surface temperature in the Tropics. *J. Climate*, **6**, 1898–1912.

Zhang, J. G., and N. A. McFarlane, 1995: Sensitivity of climate simulations to the parameterization of cumulus convection in the Canadian Climate Centre general circulation model. *Atmos.-Ocean*, **33**, 407–446.

Zhang, M. H., and Coauthors, 2005: Comparing clouds and their seasonal variations in 10 atmospheric general circulation models with satellite measurements. *J. Geophys. Res.*, 110(D15):S02, doi:10.1029/2004GD005021.